RSC Advances

PAPER

View Article Online
View Journal | View Issue

Cite this: *RSC Adv.*, 2022, **12**, 3465

Estimations of $Fe^{0/-1}$–N_2 interaction energies of iron(0)-dicarbene and its reduced analogue by EDA-NOCV analyses: crucial steps in dinitrogen activation under mild conditions†

Sai Manoj N. V. T. Gorantla and Kartik Chandra Mondal *

Metal complexes containing low valence iron atoms are often experimentally observed to bind with the dinitrogen (N_2) molecule. This phenomenon has attracted the attention of industrialists, chemists and bio-chemists since these N_2-bonded iron complexes can produce ammonia under suitable chemical or electrochemical conditions. The higher binding affinity of the Fe-atom towards N_2 is a bit 'mysterious' compared to that of the other first row transition metal atoms. Fine powders of α-Fe^0 are even part of industrial ammonia production (Haber–Bosch process) which operates at high temperature and high pressure. Herein, we report the EDA-NOCV analyses of the previously reported dinitrogen-bonded neutral molecular complex $(cAAC^R)_2Fe^0$–N_2 (**1**) and mono-anionic complex $(cAAC^R)_2Fe^{-1}$–N_2 (**2**) to give deeper insight of the Fe–N_2 interacting orbitals and corresponding pairwise intrinsic interaction energies ($cAAC^R$ = cyclic alkyl(amino) carbene; R = Dipp or Me). The Fe^0 atom of **1** prefers to accept electron densities from N_2 *via* σ-donation while the comparatively electron rich Fe^{-1} centre of **2** donates electron densities to N_2 *via* π-backdonation. However, major stability due to the formation of an Fe–N_2 bond arises due to Fe $\rightarrow$ N_2 π-backdonation in both **1** and **2**. The $cAAC^R$ ligands act as a charge reservoir around the Fe centre. The electron densities drift away from cAAC ligands during the binding of N_2 molecules mostly *via* π-backdonation. EDA-NOCV analysis suggests that N_2 is a stronger π-acceptor rather than a σ-donor.

Received 14th November 2021
Accepted 14th December 2021

DOI: 10.1039/d1ra08348a

rsc.li/rsc-advances

Introduction

Different forms of energy can be argued as the ingredients of life.[1] Energy, life and information are linked to each other.[2] Nitrogen is one of the most common and most essential elements for the sustainability of living organisms, plants and animals. The earth's atmosphere is mostly dominated (78%) by dinitrogen gas (N_2) and yet most of the living organisms, plants and animals cannot directly utilize it according to their needs.[3] This is due to the extreme inertness and non-polar nature of kinetically stable N_2 molecules. The reduction of N_2 to ammonia (NH_3) and/or to other forms of N-containing compounds such as amino acids, nucleoside, nucleotides and most importantly peptides are keys to the existence of life on earth.[4] Thermodynamically, reduction of areal N_2 to relatively more stable NH_3 is exothermic (-46 kJ mol^{-1} at 298 K). However, the binding of N_2 and followed by activation of the N≡N bond is challenging to chemists and bio-chemists. Interestingly, a few microorganisms in the nature have found a way to solve the problem[5] providing around hundred twenty megatons of nitrogen source per year by nitrogen fixation. It is associated with some leguminous plants, like clover, beans, peas, alfalfa, lentils and lupins.[6] The enzyme called nitrogenase possesses a bimetallic inorganic core $V/Mo–Fe_7S_9C^{1-}$ (co-factor) which is responsible for N_2 binding in the reduced state.[7,8] It catalytically produces ammonia *via* reductive protonation either by 'distal' or 'alternative' pathways with the loss of hydrogen gas during this process.[7,8] The exact nature and mode of the dinitrogen binding and activation have not yet fully clear. N-containing nutrients are essential for the human race on the earth. Humans adopted domestic cultivation as early as 10 000 BC.[9] Fertilizers are now-a-days a must for effective cultivation. More than a century ago, Haber originally utilized an osmium catalyst under high temperature and pressure to produce 125 mL of NH_3 per hour.[10] In the following years Bosch and Mittasch developed efficient $Fe_3O_4/FeO/\alpha$-Fe^0 catalyst with high surface area for industrial production of twenty tonnes of NH_3 per day in the next year at BASF company.[10,11] The catalytic efficiency of iron is further promoted with K_2O, CaO, SiO_2, and Al_2O_3. At present global annual production rate of ammonia is 174 million tonnes.[12] The actual Mittasch's catalyst ($Fe_3O_4/FeO/$

Department of Chemistry, Indian Institute of Technology Madras, Chennai 600036, India. E-mail: csdkartik@iitm.ac.in

† Electronic supplementary information (ESI) available: Tables, figures, QTAIM, and optimized coordinates. See DOI: 10.1039/d1ra08348a

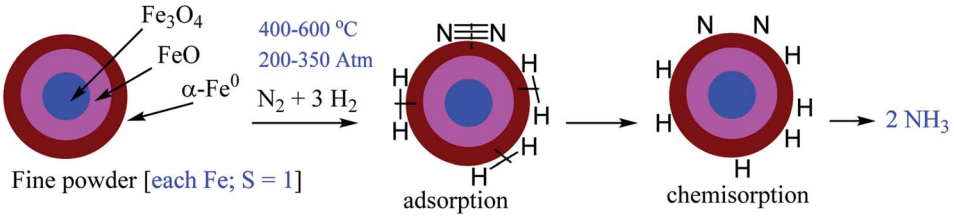

Scheme 1 Illustration of H_2 and N_2 adsorption, dissociation and formation of NH_3 in famous Haber–Bosch process showing α-Fe^0 active catalytic surface.

α-Fe^0) (Scheme 1) in Haber–Bosch catalytic cycle is the outer surface (α-Fe^0) of very reactive Fe_3O_4/FeO/α-Fe^0 particles having a body centre cubic (bcc) structure with two singly-occupied d_{z^2} and $d_{x^2-y^2}$ orbitals which do not participate in multicentre delocalized bonding with its neighbouring Fe^0 atoms.[13]

To obtain a favourable thermodynamic driving force for the reaction between N_2 and H_2 the industrial process is designed to occur at high pressure (Scheme 1). In 2007 Gerhard Ertl has been awarded the Nobel Prize in chemistry for his captivating decades long works on fundamental processes at the gas–solid interface involving Fe^0–N_2 adsorption on the α-Fe^0 surface of Fe_3O_4/FeO/α-Fe^0 catalyst. His work on 'Interaction of nitrogen with iron surfaces' clarified the long-standing confusion in Haber–Bosch process.[14] It has been found that N≡N bond dissociates on pure Fe-surfaces forming Fe_4N atomic-bilayer just above room temperature. He also explained the role of promoter K_2O in Haber–Bosch ammonia synthesis process employing photoelectron spectroscopy and other experimental techniques. The pre-adsorbed potassium on the Fe-surface removes energy barrier of dissociative nitrogen chemisorption of N_2 molecule.[15] The overall yield of NH_3 in Haber–Bosch industrial process is 97% when the unreacted gases are recycled again and again.[10] However, at present this process consumes ~2% of the total global energy supply. Additionally, it produces large amounts of greenhouse gases.[16] Alternative synthetic methods which will produce NH_3 in a much greener way are highly desired.[17–41] Low valence and/or low valent metal complexes[17–33,37–41] and low coordinate boron–carbene[34–36] compounds are found to bind N_2 which can be activated to obtain NH_3 or N_2H_4 under milder conditions.[17–41] The reductive protonation of bonded N_2 of these complexes can lead to the formation of either NH_3 or N_2H_4 or even a mixture of both. Formation of ammonia is more common due to its higher thermodynamic stability over hydrazine. It has been stated that π-backdonation from metal to N_2 (M → N_2) are very pivotal for the weakening of strong N≡N bond. Higher the electron densities on metal atom, higher is the π-backdonation from metal to N_2 (Scheme 2). However, there is no report on the estimation of M–N_2 interaction energies in a stable/isolable complex showing the extent of π-backdonation from M → N_2 and σ-donation from N_2 → M (M = transition metal; Scheme 2).[42] The energy decomposition analysis-natural orbital for chemical valence (EDA-NOCV)[43] analysis is a very powerful tool that can be employed for the estimation of intrinsic interaction energy (ΔE_{int}) and pairwise orbital interaction energy ($\Delta E_{orb(n)}$). The triple bond of the free dinitrogen (N_2) molecule is extremely strong. EDA-NOCV analysis of free N_2 revealed that 30% of the total interaction energy between two N-atoms is only contributed by electrostatic energy (ΔE_{elstat}). The remaining 70% is orbital interaction energy (ΔE_{orb}) which is due to the covalent character of triple bond of N_2 with zero dipole moment.[43,44] The Pauli repulsion energy (ΔE_{Pauli}) between two interacting N-atoms is quite high due to repulsion between the electron clouds with similar spins (N–N = 1.102 Å). The Wiberg bond order has been computed to be 3.03. The orbital interaction energy (ΔE_{orb}) is actually due to the covalent interactions in both σ ($3\sigma_g^+$) + π ($1\pi_u$) bonds. The former is 65.6% while the latter is nearly half (34.4%) of the former. They together (σ + π) give total orbital interaction energy (ΔE_{orb}).[43,44] Point to be noted that degenerate π*-orbitals ($1\pi_g$) of N_2, which are composed of p_x and p_y atomic orbitals, are high lying in energies ($1\pi_g$; LUMO). The LUMO+1 is σ* orbital ($3\sigma_u^+$) and HOMO is N–N σ orbital ($3\sigma_g^+$) of N_2.[43,44]

Several metal complexes with low valence iron atoms containing coordinated N_2 have been synthesized, isolated and characterized by X-ray single crystal structure determination.[18–21,27–33,40,41] Additionally, they have been studied by different spectroscopic methods to shed light on their electronic structures. NBO calculations have been carried out to correlate the N–N bond lengths with those of experimentally obtained values to give emphasis on weakening of N–N bond due to M → N_2 backdonation.[18–21,27–33,40,41] However, there is till now no report[42] on the exact nature of the M–N_2 bonds and on their corresponding interaction energies (M = Fe and other transition metal) of stable/isolable dinitrogen bonded metal complexes. Herein, we report on the DFT, NBO, QTAIM calculations and EDA-NOCV analysis of previously reported dinitrogen-bonded $(cAAC^R)_2Fe^0$–N_2 (**1**) and $(cAAC^R)_2Fe^{-1}$–N_2 (**2**) complexes[41] to give a deeper insight into the nature of M–N_2 bonds and corresponding pairwise interaction energies ($cAAC^R$ = cyclic alkyl(amino) carbene; R = Dipp[41] or Me for our theoretical studies). The role of non-innocent cAAC ligands has also been discussed here.

Results and discussion

The spin of each Fe-atom of ferromagnetic α-iron metal is S = 1.[10] The spin ground state of $(cAAC^{Dipp})_2Fe^0$ has been confirmed to be S = 1 by EPR and ^{57}Fe Mössbauer spectroscopy by Peters *et al.*[45] Additionally, they have experimentally shown[41] (by UV/vis

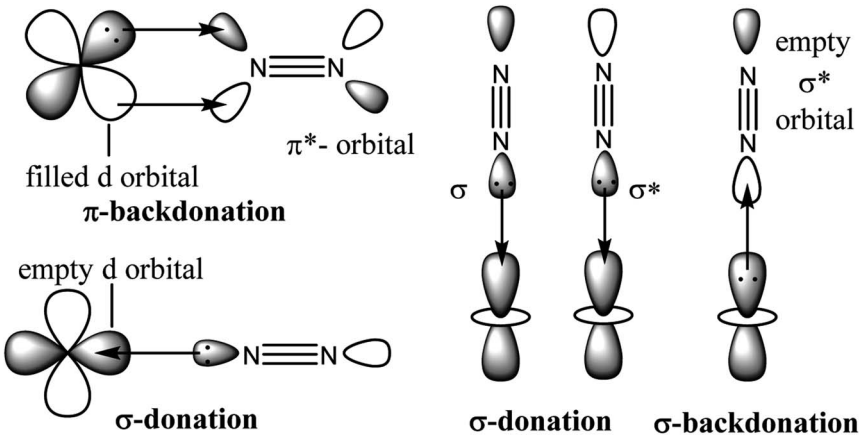

Scheme 2 End-on interactions between the orbitals metal (M) and N_2.

spectroscopy) that the N_2 binds to $(cAAC)_2Fe^0$ in end-on fashion. This N_2 binding at Fe-centre is highly temperature sensitive (<−80 °C).[41] Experimentally the authors have isolated the elusive anionic $(cAAC^{Dipp})_2Fe^{-1}$–N_2 species by reducing *in situ* formed precursor $(cAAC^{Dipp})_2Fe^0$–N_2 (**1′**) with KC_8 in the presence of 18-crown-6 ether below −95 °C with the chemical composition of $[(cAAC^{Dipp})_2Fe(N_2)][K(18\text{-crown-6})]$ (**2′**) (Scheme 3). The latter species (**2′**) has a ground state $S = \frac{1}{2}$ confirmed by solution EPR measurements.[41] This anionic complex has further been shown to catalytically produce NH_3 below −95 °C. The reduction of dinitrogen to ammonia takes place upon treatment with N_2, KC_8 and $HBAr^F{}_4\cdot 2Et_2O$ in ether medium. Only a little has been reported about their (**1′–2′**) aspects of chemical bonding.[41]

We have modelled and optimized $(L)_2Fe^0$–N_2 as neutral (**1**; L = $cAAC^{Me}$) and anionic complexes (**2**; L = $cAAC^{Me}$) stabilized by $cAAC^{Me}$ ligands to shed light on the bonding and stability of spectroscopically observed elusive neutral $(cAAC^{Dipp})_2Fe^0$–N_2 (**1′**; $cAAC^{Dipp}$) and crystallographically characterized $[(cAAC^{Dipp})_2Fe^{-1}(N_2)][K(18\text{-crown-6})]$ complexes (**2′**) reported by

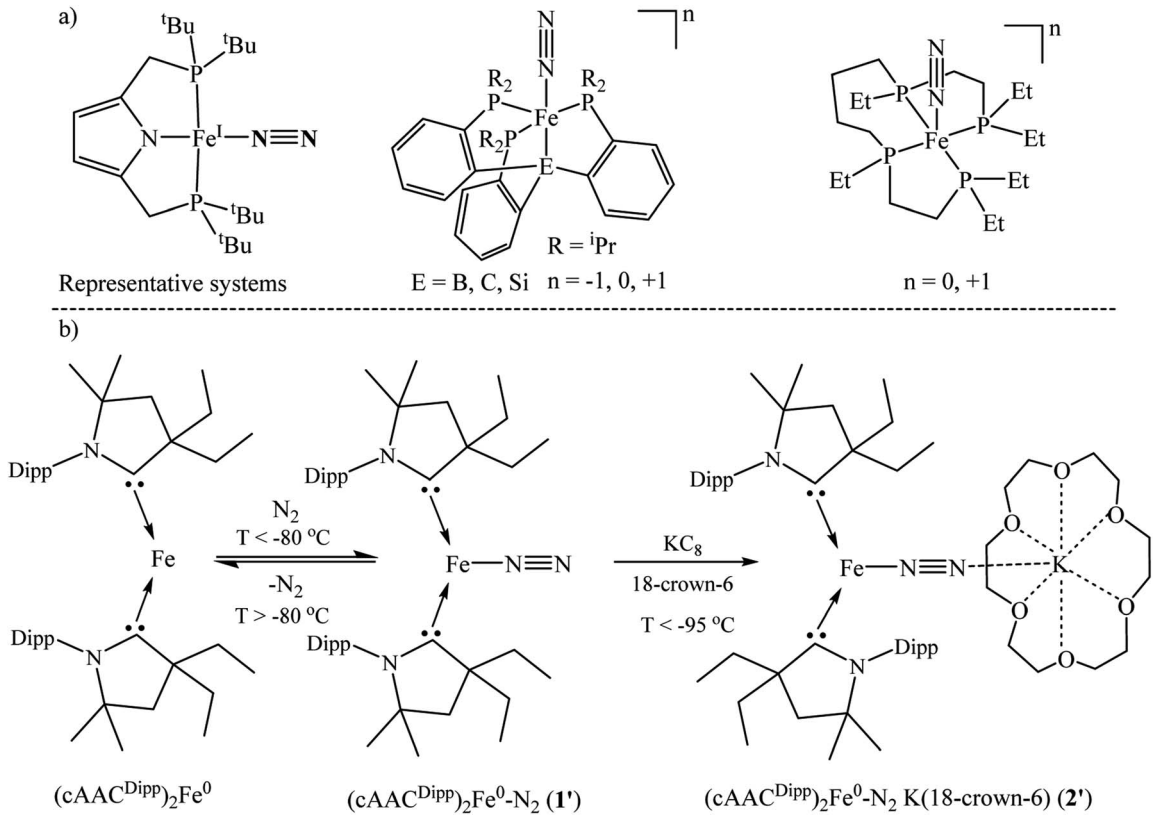

Scheme 3 Representative Fe–N_2 containing iron complexes.[17,18,38,40,41,45]

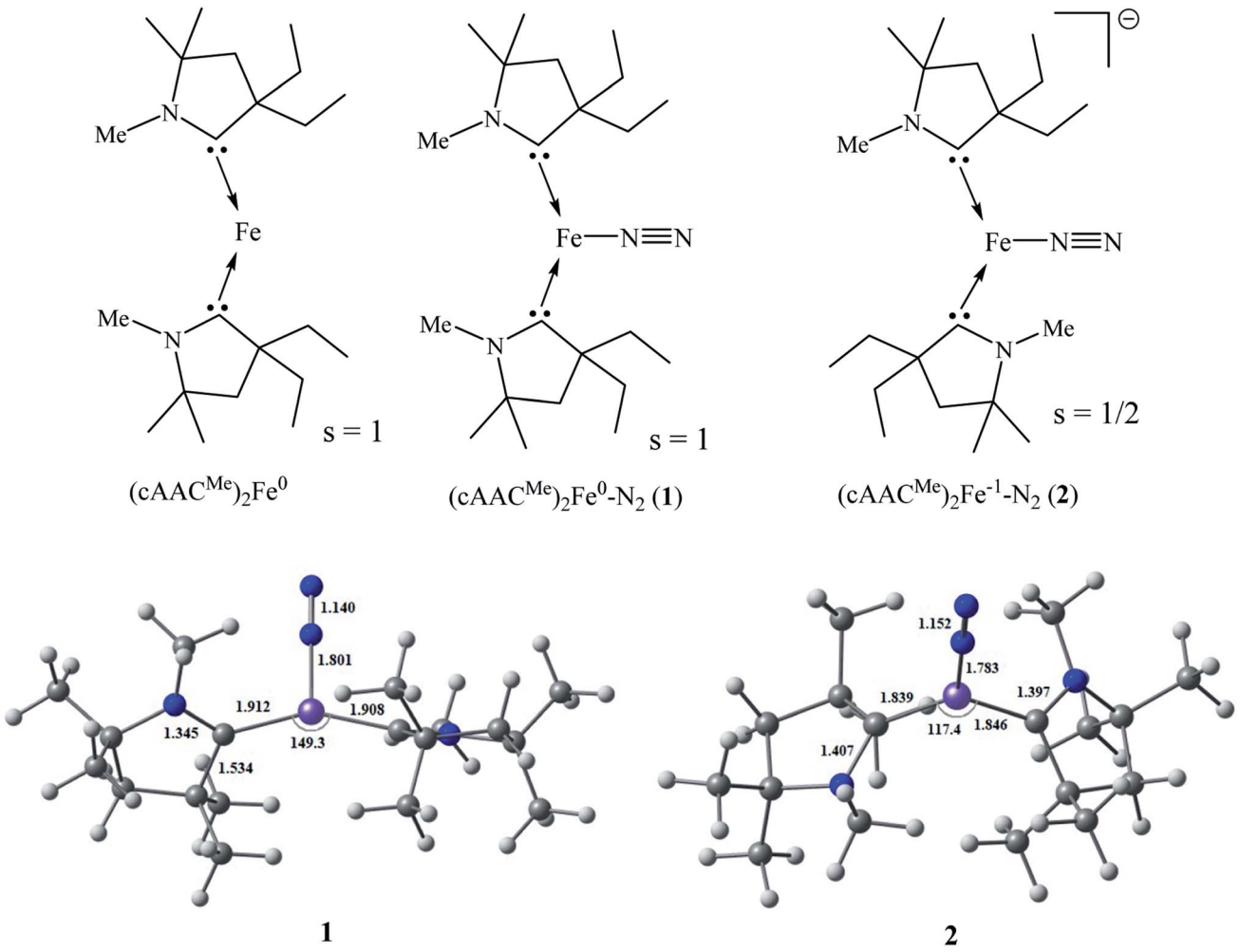

Fig. 1 Optimized geometries of complex **1** in triplet state (s = 1) and mono-anionic complex **2** in doublet state (s = 1/2) at BP86-D3(BJ)/Def2-TZVPP level.

Jonas Peters and co-workers. The Fe–N bond distance of $[(cAAC^{Dipp})_2Fe(N_2)][K(18\text{-crown-6})]$ is 1.777 Å while the N–N bond length of the bonded N_2 is 1.035(4) Å which is slightly shorter than that of the free N_2 (1.102 Å) molecule. X-ray crystallography of the complex **2′** revealed that Fe-centre adopted a distorted trigonal planar coordination geometry.[41]

The modelled neutral $(cAAC^{Me})_2Fe–N_2$ complex (**1**) has been optimized in singlet (Fig. S1†), triplet (Fig. 1) and quintet electronic states (Fig. S1†). The calculations at BP86-D3(BJ)/Def2TZVPP level of theory in the gas phase suggest that triplet state is more stable by 11.53 and 20 kcal mol^{-1} over singlet and quintet states, respectively. The N–C–C–N torsion angle of 37.7° in complex **1** suggests that the two cAAC ligands are relatively perpendicular to each other, while the C–Fe–C bond angle of 149.3° shows that the geometry is lightly bent compared to that of $(cAAC)_2Fe^0$ containing a two coordinate Fe^0 atom with C_{cAAC}–Fe–C_{cAAC} bond angle of 169.52(5)°.[45] The Fe–N and N–N bond lengths of the simplified complex **1** are 1.801 Å and 1.140 Å respectively (with Me-group on N-atom of cAAC ligand). The two cAAC ligands are almost equidistant from the central Fe atom with a minor difference (Fig. 1). In contrast to the Fe–Mo cofactor (FeMoco) of nitrogenase enzyme,[7,8] the two coordinate $(cAAC)_2Fe$ can bind to N_2 even in resting condition below −80°[41] or in other words without the external supply of electrons.

Upon reduction, the geometry becomes more bent in complex **2** as indicated by the C_{cAAC}–Fe–C_{cAAC} bond angle of 117.4° (Fig. 1). This differs from the C–Fe–C bond angle (140.8°) of experimentally isolated $[(cAAC^{Dipp})_2Fe(N_2)][K(18\text{-crown-6})]$ (**2′**) due to to the steric effects of two $cAAC^{Dipp}$ ligands. We can reason the reduction in C–Fe–C bond angle in the modelled complex to the presence of less bulky substituents on cAAC ligand which reduces the steric repulsion. This reduction in C–Fe–C bond angle also slightly lower the C–Fe bond lengths in complex **2** compared to that of the reported structure. The Fe–N bond distance of modelled complex **2** (1.782 Å) correlated well with the reported value of 1.777 Å (**2′**). The geometrical parameters calculated at BP86-D3(BJ)/Def2TZVPP level agrees well with the experimental values with no major discrepancies. However, we have also performed geometry optimization of complexes **1** and **2** at the TPSS-D3(BJ)/Def2TZVPP and PW6B95-D3/Def2TZVPP level to compare and support the results. While

the Fe–N bond lengths of complexes **1** and **2** calculated at TPSS-D3(BJ) level are 1.808 Å, 1.782 Å respectively (Fig. S1†), the calculated N–N bond lengths are 1.136 and 1.149 Å (Fig. S1†). The geometrical parameters calculated at TPSS-D3(BJ) match well with the results of the BP86-D3(BJ) level. However, the Fe–N bond lengths (1.899 and 1.864 Å) calculated at PW6B95-D3 level (Fig. S1†) differ significantly with those calculated at TPSS-D3(BJ), BP86-D3(BJ) and also experimental values. The calculated C–Fe–C bond angle of complex **2** at TPSS-D3(BJ) is also acute (120.7°), supporting the reason for the difference from the experimental bond angle as mentioned above. The N–C–C–N torsion angle of 145.1° indicates that the two carbene ligands are slightly more *trans* to each other in complex **2**. The coordination geometries of Fe-centres reveal that both complexes **1** and **2** possess a distorted trigonal planar geometry as indicated by Σ_{angle} of 359.8° and 359.9° respectively and are in agreement with the reported structure (**2′**).[41] The longer C–N bond lengths of 1.343–1.345 Å in complex **1** and 1.397–1.407 Å in complex **2** than that of 1.315(3) Å in free carbene, indicate spin delocalization onto ligands (C_{cAAC} ← Fe).[46] The dissociation of $(cAAC^{Me})_2Fe–N_2$ bond [$(cAAC^{Me})_2Fe–N_2$ → $(cAAC^{Me})_2Fe + N_2$] in complex **1** and **2** is slightly endothermic (ΔG^{298} = 18.9–29.6 kcal mol^{-1}) and the energy of dissociation is 30.1–40.26 kcal mol^{-1} (bond enthalpy) respectively. The electron affinity of **1** is 13.74 kcal mol^{-1}.

We have employed charge and energy density methods like natural bond orbital (NBO), quantum theory of atoms in molecules (QTAIM) and energy decomposition analysis coupled with natural orbitals for chemical valence (EDA-NOCV) methods to study the nature of the Fe–N bond. The Wiberg bond index (WBI) of 0.82 (**1**), 0.92 (**2**) for Fe–N bond and 2.53 (**1**), 2.43 (**2**) for N–N bond of **1** and **2**, respectively (Table 1). The Fe–N and N–N bond orders are consistent with the Fe–N and N–N bond lengths of both the complexes. The N–N bond orders (BO; 2.53 (**1**), 2.43 (**2**)) of N_2 in complexes **1** and **2** are significantly smaller than those of free N_2 molecule (BO = 3.03). This indicates the weakening of the N–N bond *via* π-backdonation after the binding of N_2 with Fe-centres which is crucial for the activation of N_2. Previous temperature dependent UV/vis studies showed that N_2 binding at Fe^0 centre could only happen below −80 °C.[41] The computational results show that the spin density of the Fe–N bond with an electron occupancy of 0.99 is mostly concentrated on N-atom (80.6%) for complex **1**. The calculation does not show bond occupancy for the Fe–N bond of complex **2**. The C_{cAAC}–Fe bonds of complex **1** and **2** show two occupancies representing σ- and π-interactions with spin density mostly concentrated on C_{cAAC} (62.9–71.5%) for σ-interactions and Fe (68.4–75.3%) for π-interactions (Table 1). The natural charge distribution of $(cAAC^{Me})_2Fe^0$ shows a negative charge on cAAC ligands and a positive charge on the Fe-atom suggesting π-backdonation (Fe → N_2) is stronger than σ-donation (N_2 → Fe). Upon binding to N_2, the cAAC ligands develop a positive charge and the Fe-center of **1** shows an increase in positive charge as well, while the N_2 ligand accumulates a negative charge, suggesting N_2 is stronger π-acceptor than a σ-donor. This indicates that the charge transfer occurs in the direction cAAC → Fe → N_2. It is well known that cAAC is a non-innocent ligand.[46b,c] It can control the charge flow and distribute the electron densities distributions based on the electronic situations and or requirement. Whereas the negative charge on cAAC, Fe and N_2 of complex **2** suggests the delocalization of one electron-charge upon reduction of **1**. The α-SOMO and α-SOMO−1 of complex **1** represent the two unpaired electrons residing in d_{xy} and $d_{x^2-y^2}$ of the triplet state. The α-SOMO−1 shows π-interaction of $d_{x^2y^2}$ orbital of Fe and lone pair on cAAC ligand with π_x-orbital of N_2, while α-SOMO−2 indicates π-interaction of d_{yz} orbital of Fe-atom with π_y-orbital of N_2 (Fig. S2†). Whereas α-SOMO of complex **2** represents an unpaired electron in d_{xz} orbital of Fe showing small amount of interaction with π_x orbital of N_2. The α-SOMO−1, α-SOMO−2 and α-SOMO−3 indicate the interaction of $d_{x^2-y^2}$, d_{z^2} and d_{yz} orbitals of Fe with π_x and π_y orbital of N_2 (Fig. S3†). The QTAIM analysis shows a bond path (Fig. S4†) and considerable electron density $\rho(r)$ along the Fe–N bond path in both complexes **1** and **2** (Table 2). Little increase in $\rho(r)$ along Fe–N and C_{cAAC}–Fe bond paths in complex **2** corroborates the delocalization of electron density and agrees with the charge distribution from NBO analysis. The ellipticity ($\varepsilon_{BCP} = \lambda_1/\lambda_2 - 1$)

Table 2 AIM results of the $(cAAC)_2Fe–N_2$ bonds of complex **1** and anionic complex **2** at the BP86-D3(BJ)/Def2-TZVPP level of theory. (The values are in a.u.)

Bond	$\rho(r)$	$\nabla^2\rho(r)$	$H(r)$	$V(r)$	$G(r)$	ε_{BCP}
Fe–N(**1**)	0.131	0.796	−0.039	−0.277	0.238	0.248
C–Fe(**1**)	0.124	0.342	−0.056	−0.196	0.140	0.318
Fe–N(**2**)	0.139	0.793	−0.046	−0.290	0.244	0.383
C–Fe(**2**)	0.142	0.376	−0.072	−0.237	0.165	0.107

Table 1 NBO results of the $(cAAC)_2Fe–N_2$ bonds of complexes **1** and **2** at the BP86-D3(BJ)/def2-TZVPP level of theory. Occupation number ON, polarization and hybridization of the $(cAAC)_2Fe–N_2$ bonds and partial charges *q*

Complex	Bond	ON	Polarization and hybridization (%)		WBI	q_{Fe}	q_{N_2}	q_{cAAC}
1	Fe–N	0.99	Fe: 19.4 s(21.3),p(19.4),d(59.3)	N: 80.6 s(58.4), p(41.6)	0.82	0.440	−0.122	0.144
	C–Fe	0.96	Fe: 28.5 s(20.0), p(13.8), d(66.2)	C: 71.5 s(41.8), p(58.2)	0.84			
		0.91	Fe: 75.3 s(0.0), p(4.7), d(95.3)	C: 24.7 s(0.8), p(99.2)				
2	Fe–N	—	—	—	0.92	−0.223	−0.275	−0.510
	C–Fe	0.97	Fe: 37.1 s(20.6), p(8.3), d(71.1)	C: 62.9 s(45.3), p(54.7)	1.09			
		0.90	Fe: 68.4 s(0.8), p(7.5), d(91.7)	C: 31.6 s(0.2), p(99.8)				
$(cAAC)_2Fe$	C–Fe	0.91	Fe: 14.6 s(42.5), p(50.0), d(7.5)	C: 85.4 s(39.5), p(60.5)	0.88	0.245	—	−0.244
		0.90	Fe: 98.9 s(0.4), p(0.2), d(99.4)	C: 1.1 s(5.6), p(94.4)				

is a measure of bond order and in general, the ε_{BCP} of a single and triple bond is close to zero because of cylindrical contours of electron density ρ, while for double bond the value is greater than zero.[47] This is due to the asymmetric distribution of electron density ρ perpendicular to the bond path for a double bond. The ellipticity (ε) values of 0.248 and 0.383 for the Fe–N bond of complexes **1** and **2** suggests the possible multiple bond character.

The EDA-NOCV method[48] is more appropriate in explaining the nature of the bond as one of the major strengths of the method is its ability to provide the best bonding model to represent the bonding situation in the equilibrium geometries.[48] To give the best bonding description of Fe–N bond by EDA-NOCV method, we have considered neutral $(cAAC^{Me})_2Fe$ fragment in electronic triplet state and neutral N_2 fragment in electronic singlet state ($1\Sigma_g^+$) for complex **1** and mono-anionic $[(cAAC^{Me})_2Fe]^-$ fragment in electronic doublet state and neutral N_2 fragment in electronic singlet state ($1\Sigma_g^+$) for complex **2** (Table 3). The instantaneous interaction (ΔE_{int}) demonstrates the strength of the bond and ΔE_{int} for Fe^0-complex **1** (87.9 kcal mol^{-1}) is significantly higher than that of Fe^{-1}-complex **2** (63.8 kcal mol^{-1}). This lowering of instantaneous interaction is favourable as the reduced Fe^{-1}-complex **2** is the active species in the catalytic conversion of $N_2 \rightarrow NH_3$ in the presence of strong proton donor. Note that the instantaneous interactions in **1** and **2** are moderately higher than their bond dissociation energies and the difference can be attributed to the preparative energy. The preparative energies emanate from the modifications in the geometry of the fragments from their equilibrium structure to the geometry in the compound and also from the electronic excitation to a reference state. The orbital (covalent) interactions marginally dominate the total attractive interactions in both complexes **1** (57.9%) and **2** (53.2%). The Fe–N bond of **1** is slightly more covalent in nature than that of **2**. The electrostatic interactions contribute 40.2–45% and dispersion contribution provide 1.8–1.9% to the total attractive interactions (Table 3). We optimized complex **1** in diethyl ether solvent (see ref. 41) using the CPCM solvation model and performed an EDA-NOCV calculation to check the effect of the solvent on the bond strength (ΔE_{int}). Interestingly, the results show that the effect of solvent is minimal and showed imperceptible differences in the bonding parameters like intrinsic interactions (87.5 kcal mol^{-1}) and orbital interactions (−159.7 kcal mol^{-1}) compared to that of the gas phase (87.9 and 161 kcal mol^{-1}) (Table S1†).

The total orbital interactions can further be broken down into pairwise contributions which can shed light on the type of interactions (Table 3). The deformation densities and the associated molecular orbitals provide insight into the direction of charge flow as shown in Fig. 2 and 3. The first orbital term (ΔE_{orb1}) of complex **1** represents the σ-electron donation (Fe ← N_2) from HOMO ($3\sigma_g^+$) of N_2 into vacant d-type anti-bonding orbital (LUMO; mixture of p_z orbitals of C_{cAAC} and d-orbital of Fe^0 of **1**) of $(cAAC)_2Fe^0$ along with the slight charge transfer from d_{xz} orbital (HOMO−2) of Fe and contributes 38% of the total orbital interactions. The deformation densities of Fig. 2 (top, left) show charge flow from red region on N_2 to blue region on $(cAAC)_2Fe^0$. The second and third orbital terms (ΔE_{orb2-3}) designates π-backdonations (Fe → N_2) from hybrid d_{z^2}–$d_{x^2\ y^2}$ orbital (HOMO) of Fe into vacant degenerate π* orbital LUMO ($1\pi_g$) of N_2 and partly into SOMO (d_{yz}) of Fe center and from d_{xz} orbital (HOMO−1) of Fe into vacant degenerate π* orbital LUMO′ ($1\pi_g'$) of N_2 in second and third orbital terms respectively. The π-backdonations together contribute 53.9% to the total orbital interactions (Table 3). The weaker fourth orbital term (4.6%) is due to σ-electron donation (Fe ← N_2) from HOMO−2 ($2\sigma_u^+$) of N_2 into vacant d-type orbital (LUMO) of Fe and the two Fe ← N_2 σ electron donations (ΔE_{orb1}, ΔE_{orb4}) together contribute 42.6% (Fig. 2) of **1**. Table 3 shows that the $Fe^0 \rightarrow N_2$ π-backdonation (ΔE_{orb2-3}) in **1** is nearly 10% higher than σ-donation ($\Delta E_{orb1,4}$). The fluctuations of electron clouds

Table 3 The EDA-NOCV results at the BP86-D3(BJ)/TZ2P level of $(cAAC)_2Fe–N_2$ bonds of complexes **1** and **2** using neutral $(cAAC)_2Fe$ in electronic triplet state and neutral N_2 fragment electronic singlet state as interacting fragments for complex **1** and singly charged $[(cAAC)_2Fe]^-$ in electronic doublet state and neutral N_2 fragment electronic singlet state as interacting fragments for complex **2**. Energies are in kcal mol^{-1}

Energy	Interaction	$(cAAC)_2Fe$ (T) + $[N_2]$ (S); (**1**)	$[(cAAC)_2Fe]^-$ (D) + $[N_2]$ (S); (**2**)
ΔE_{int}		−87.9	−63.8
ΔE_{Pauli}		190.2	164.1
ΔE_{disp} [a]		−5.2 (1.9%)	−4.1 (1.8%)
ΔE_{elstat} [a]		−111.9 (40.2%)	−102.4 (45.0%)
ΔE_{orb} [a]		−161.0 (57.9%)	−121.4 (53.2%)
$\Delta E_{orb(1)}$ [b]	$(cAAC)_2Fe \leftarrow N_2$ σ-donation	−61.4 (38.1%)	
	$(cAAC)_2Fe \rightarrow N_2$ π-backdonation		−39.4 (32.4%)
$\Delta E_{orb(2)}$ [b]	$(cAAC)_2Fe \rightarrow N_2$ π-backdonation	−53.6 (33.3%)	−34.0 (28.0%)
$\Delta E_{orb(3)}$ [b]	$(cAAC)_2Fe \rightarrow N_2$ π-backdonation	−33.2 (20.6%)	−25.2 (20.8%)
$\Delta E_{orb(4)}$ [b]	$(cAAC)_2Fe \leftarrow N_2$ σ-donation	−7.5 (4.6%)	−14.7 (12.1%)
$\Delta E_{orb(rest)}$ [b]		−5.3 (3.3%)	−8.1 (6.7%)

[a] The values in the parentheses show the contribution to the total attractive interaction $\Delta E_{elstat} + \Delta E_{orb} + \Delta E_{disp}$. [b] The values in parentheses show the contribution to the total orbital interaction ΔE_{orb}.

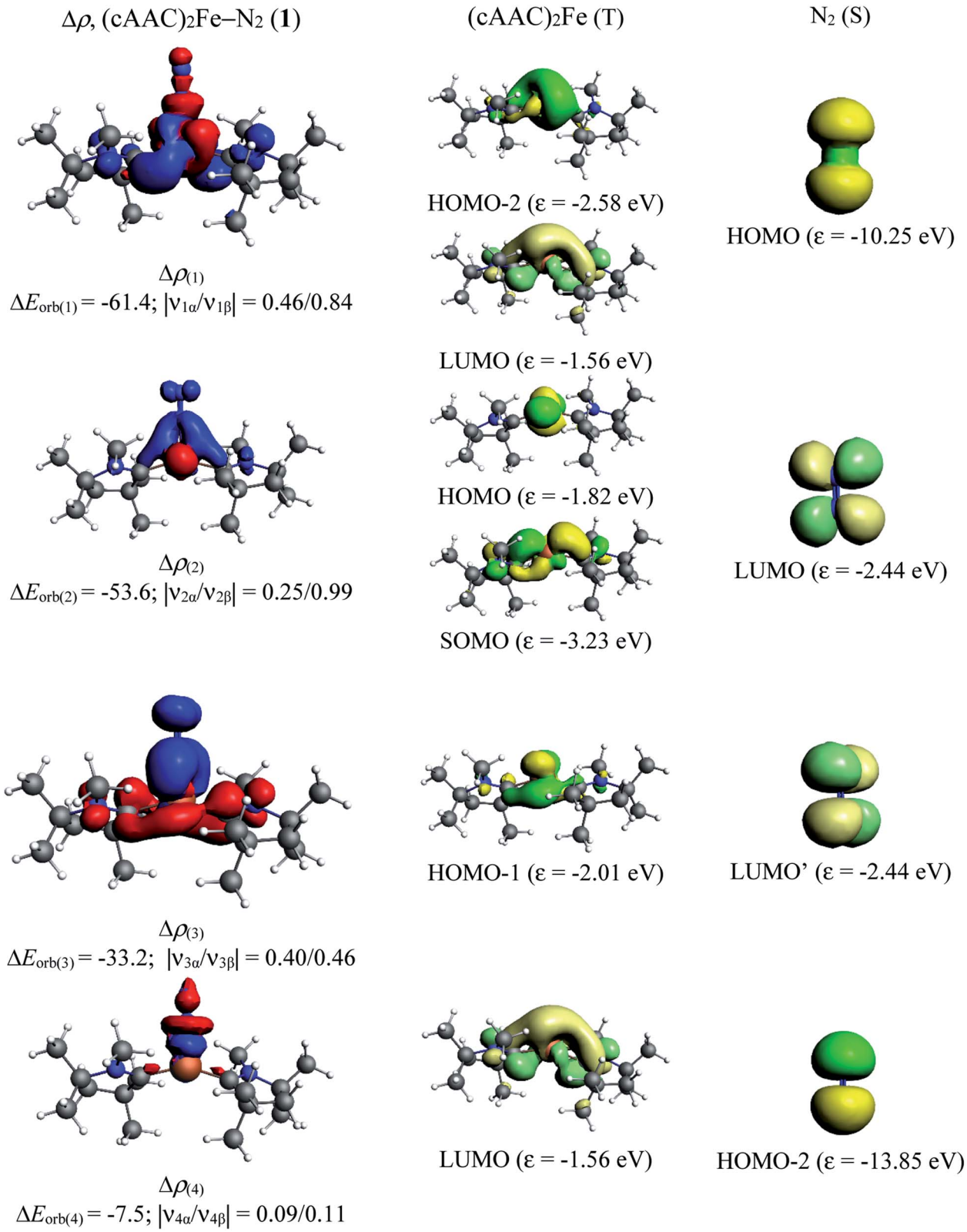

Fig. 2 The shape of the deformation densities $\Delta\rho_{(1)-(4)}$ that correspond to $\Delta E_{orb(1)-(4)}$, and the associated MOs of $(cAAC)_2Fe-N_2$ (**1**) and the fragments orbitals of $(cAAC)_2Fe$ in triplet state and N_2 in the singlet state at the BP86-D3(BJ)/TZ2P level. Isosurface values of 0.003 au for $\Delta\rho_{(1-4)}$. The eigenvalues $|\nu_n|$ give the size of the charge migration in *e*. The direction of the charge flow of the deformation densities is red → blue. Energies are in kcal mol^{-1}.

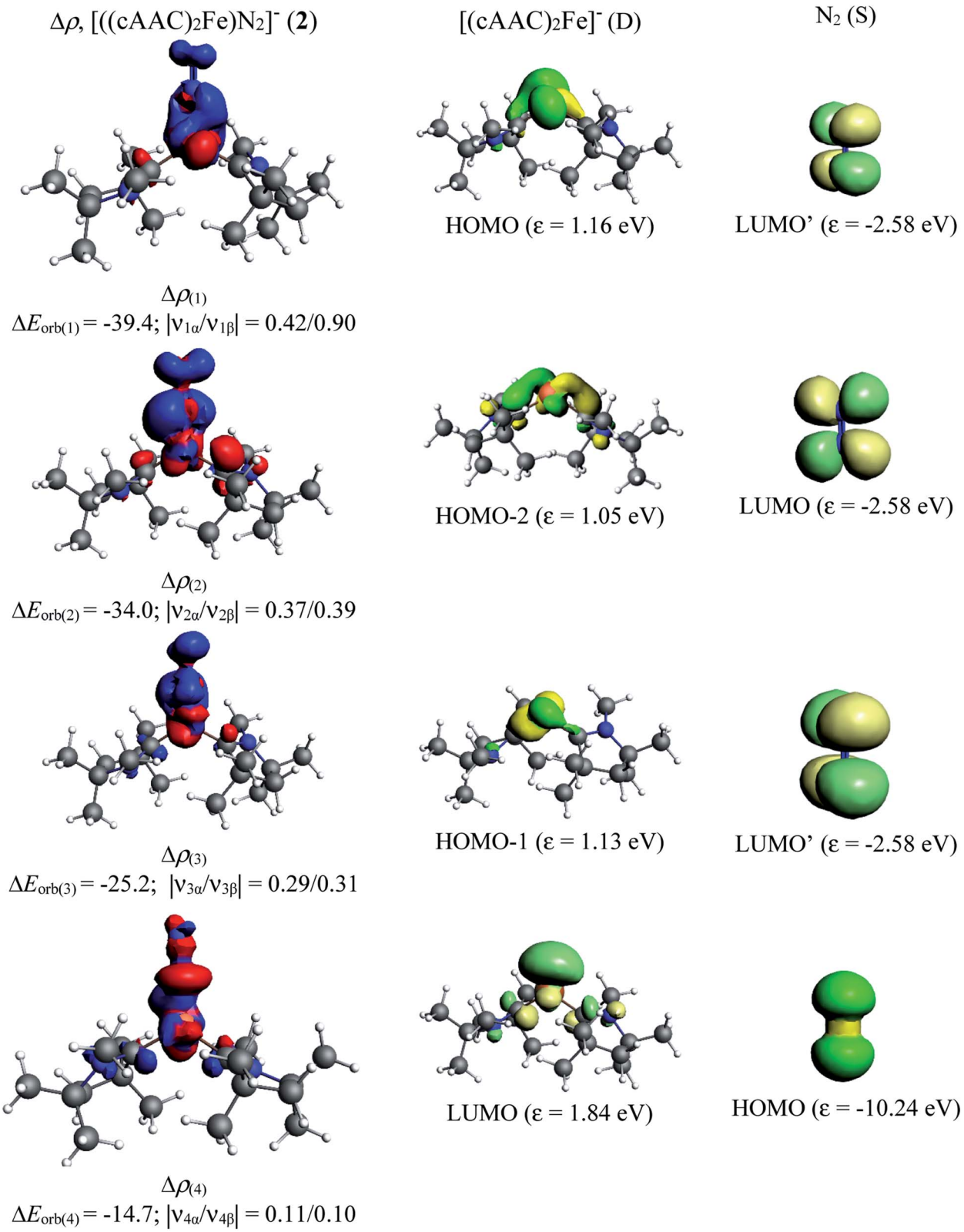

Fig. 3 The shape of the deformation densities $\Delta\rho_{(1)-(4)}$ that correspond to $\Delta E_{orb(1)-(4)}$, and the associated MOs of $[((cAAC)_2Fe)N_2]^-$ (**2**) and the fragments orbitals of $[(cAAC)_2Fe]^-$ in doublet state and N_2 in the singlet state at the BP86-D3(BJ)/TZ2P level. Isosurface values of 0.003 au for $\Delta\rho_{(1-4)}$. The eigenvalues $|\nu_n|$ give the size of the charge migration in *e*. The direction of the charge flow of the deformation densities is red → blue. Energies are in kcal mol^{-1}.

on cAAC ligands during the formation of σ- and π-bonds as expected since cAAC is known as both σ-donor and π-acceptor.[46]

In contrast, the first three orbital terms (ΔE_{orb1-3}) of complex **2** represent π-electron backdonations (Fe → N_2). While the first orbital term (ΔE_{orb1}) comes from the π-electron backdonation from d_{z^2} orbital (HOMO) of Fe^{-1} into degenerate vacant $\pi(p_y)^*$ orbital (LUMO′) of N_2, the second orbital term (ΔE_{orb2}) is due to π-backdonation from $d_{x^2y^2}$ orbital (HOMO-2) into vacant degenerate π* orbital (LUMO) ($1\pi_g$) of N_2. The third orbital term (ΔE_{orb3}) is due to π-backdonation from d_{yz} orbital (HOMO−1) of Fe^{-1} into vacant degenerate π* orbital LUMO′ ($1\pi_g^{'}$) of N_2. The three π-backdonations together contribute 81.2% of the total orbital contributions. The fourth orbital term (ΔE_{orb4}) represents the σ electron donation (Fe ← N_2) from HOMO ($3\sigma_g^{+}$) of N_2 into vacant d-type orbital (LUMO) of Fe and contributes 12.1% to the total orbital interactions (Fig. 3). It is to be observed that due to the mixing of orbitals of cAAC ligand, the shapes of d orbitals of Fe are slightly deformed and can be seen from the associated molecular orbitals of [$(cAAC^{Me})_2Fe$] fragment in Fig. 2 and 3. The mixing of the p_z-orbital of cAAC ligands with d-orbitals of Fe-centre of **1** is much higher than that of **2**.

Overall, Fe → N_2 π-backdonations are stronger than Fe ← N_2 σ-donations in both complexes **1** and **2**. The percentage of Fe → N_2 π-backdonation in **2** is nearly one and half times higher than that of **1** and Fe ← N_2 σ-donation in **2** is over nearly four times lower than that of **1**. A close look at the deformation densities (Fig. 2 and 3) in **1–2** suggests that electronic effect of cAAC ligands is much lower in **2** than in **1** during the formations of σ- and π-bonds. The matrix isolated triplet $M(N_2)_8$ (M = Ca, Sr, Ba) species are also mainly stabilized by $[M(d_\pi)] \rightarrow (N_2)_8$ π-backdonation.[42] The EDA-NOCV results, in particular, the σ-donation and π-backdonations and the ellipticity values of QTAIM agrees well with each other and ascertain the speculation of the authors that "the ability of $[(CAAC)_2Fe]/[(CAAC)_2Fe(N_2)]$ to perform nitrogen fixation may arise from the relative flexibility of the system, which is capable of switching between two- and three-coordinate geometries, and allows the formation of highly covalent Fe–N_2 multiple-bond interactions".[41]

In conclusion, although a plethora of iron complexes are shown to bind N_2 molecules in past. The nature of the bonding interactions between Fe-centre and N_2 molecule has not been studied by EDA-NOCV. This study for the first time has provided a quantitative and detailed illustration orbital interactions to shed light on the engrossing Fe–N_2 bond. The bonding interactions between $(L)_2Fe^n$ ($n = 0, -1$) and N_2 fragments of two low coordinate and low valence Fe-complexes have been studied by DFT, NBO, QTAIM and EDA-NOCV analyses which revealed that Fe → N_2 π-backdonations are major interactions for efficient N_2 binding. However, the N_2 → Fe σ-donation contributions is not negligible in both the complexes. Fe^0 center of $(L)_2Fe^0$ of **1** is a better σ-acceptor than Fe^{-1} of **2** while Fe^{-1} center of $(L)_2Fe^{-1}$ of **2** is a much stronger π-backdonor due to its richness of electron densities in the latter. The Fe–N_2 interaction energy of **1** is significantly higher than that of **2**. These two Fe-complexes are an unprecedented set of complexes among the N_2-bonded Fe-complexes[18–21,27–33,40,41] which have been studied by EDA-NOCV calculations. The role of cAAC has been clearly shown by the deformation densities during N_2 binding at Fe-centre (charge flow from red → blue). Our EDA-NOCV analysis will help the synthetic chemists to have much clearer view/understanding on the bonding interactions of captivating Fe–N_2 bond and design a superior metal-complex for efficient N_2 binding in their future studies.

Computational methods

Geometry optimizations and vibrational frequencies calculations of $(cAAC)_2Fe–N_2$ as neutral (**1**) and anionic complexes (**2**) in singlet, doublet, triplet and quintet electronic states has been carried out at the BP86-D3(BJ)/Def2TZVPP, for triplet and doublet states additionally at the TPSS-D3(BJ)/Def2TZVPP and PW6B95-D3/Def2TZVPP level[49] in gas phase. The absence of imaginary frequencies assures the minima on potential energy surface. We have also optimized complex **1** in diethyl ether solvent using CPCM solvation model.[49] All the calculations have been performed using Gaussian 16 program package.[50] NBO[51] calculations have been performed using NBO 6.0 (ref. 52) program to evaluate partial charges, Wiberg bond indices (WBI)[53] and natural bond orbitals. The nature of Fe–N_2 bonds in complexes **1** and **2** were analyzed by energy decomposition analysis (EDA)[54] coupled with natural orbital for chemical valence (NOCV)[55] using ADF 2018.105 program package.[56] EDA-NOCV calculations were carried out at the BP86-D3(BJ)/TZ2P[57] level using the geometries optimized at BP86-D3(BJ)/def2-TZVPP level. EDA-NOCV method involves the decomposition of the intrinsic interaction energy (ΔE_{int}) between two fragments into four energy components as follows:

$$\Delta E_{int} = \Delta E_{elstat} + \Delta E_{Pauli} + \Delta E_{orb} + \Delta E_{disp}, \quad (1)$$

where the electrostatic ΔE_{elstat} term is originated from the quasi-classical electrostatic interaction between the unperturbed charge distributions of the prepared fragments, the Pauli repulsion ΔE_{Pauli} is the energy change associated with the transformation from the superposition of the unperturbed electron densities of the isolated fragments to the wavefunction, which properly obeys the Pauli principle through explicit antisymmetrisation and renormalization of the production of the wavefunction. Dispersion interaction, ΔE_{disp} is also obtained as we used D3(BJ). The orbital term ΔE_{orb} comes from the mixing of orbitals, charge transfer and polarization between the isolated fragments. This can be further divided into contributions from each irreducible representation of the point group of the interacting system as follows:

$$\Delta E_{orb} = \sum_r \Delta E_r \quad (2)$$

The combined EDA-NOCV method is able to partition the total orbital interactions into pairwise contributions of the orbital interactions which is important in providing a complete picture of the bonding. The charge deformation $\Delta\rho_k(r)$, which comes from the mixing of the orbital pairs $\psi_k(r)$ and $\psi_{-k}(r)$ of the

interacting fragments, gives the magnitude and the shape of the charge flow due to the orbital interactions (eqn (3)), and the associated orbital energy ΔE_{orb} presents the amount of orbital energy coming from such interaction (eqn (4)).

$$\Delta\rho_{orb}(r) = \sum_k \Delta\rho_k(r) = \sum_{k=1}^{N/2} v_k\left[-\psi_{-k}{}^2(r) + \psi_k{}^2(r)\right] \quad (3)$$

$$\Delta E_{Orb} = \sum_k \Delta E_{orb}^k = \sum_k v_k\left[-F_{-k,-k}^{TS} + F_{k,k}^{TS}\right] \quad (4)$$

Readers are further referred to the recent reviews articles to know more about the EDA-NOCV method and its applications.[48]

Conflicts of interest

Authors do not have any conflict of interest.

Acknowledgements

We thank Prof. Gernot Frenking and Prof. K. M. S for providing computational facilities. S. M. also thank Dr S. Pan. S. M. thanks CSIR for SRF. K. C. M thanks SERB for the ECR grant (ECR/2016/000890) and IIT madras for seed grant.

References

1 J. Wrigglesworth, *Energy And Life*, CRC Press, 1997, ISBN no. 9780748404339.
2 *Exobiology: Matter, Energy, and Information in the Origin and Evolution of Life in the Universe*, ed. J. Chela-Flores and F. Raulin, 1998, ISBN no. 978-94-011-5056-9.
3 P. Holland, *Chem. Rev.*, 2020, **120**, 4919.
4 N. Lehnert, B. W. Musselman and L. C. Seefeldt, *Chem. Soc. Rev.*, 2021, **50**, 3640.
5 N. Lehnert, G. Coruzzi, E. Hegg, L. Seefeldt and L. Stein, *NSF Workshop Report: Feeding the World in the 21st Century: Grand Challenges in the Nitrogen Cycle*, National Science Foundation, Arlington, VA, Arlington, VA, 2016.
6 V. Smil, *Enriching the Earth: Fritz Haber, Carl Bosch and the Transformation of World Food Production*, MIT Press, Cambridge, 2001.
7 B. M. Hoffman, D. R. Dean and L. C. Seefeldt, *Acc. Chem. Res.*, 2009, **42**, 609.
8 J. L. Crossland and D. R. Tyler, *Coord. Chem. Rev.*, 2010, **254**, 1883.
9 M. A. Zeder, *Curr. Anthropol.*, 2011, **52**, S221–S235.
10 M. Appl, *"Ammonia", Ullmann's Encyclopedia of Industrial Chemistry*, Weinheim, Wiley-VCH, 2006, DOI: 10.1002/14356007.a02_143.pub2.
11 A. Mittasch, Bemerkungen zur Katalyse, *Ber. Dtsch. Chem. Ges. A and B Series*, 1926, **59**, 13–36.
12 P. H. Pfromm, *J. Renewable Sustainable Energy*, 2017, **9**, 034702.
13 N. N. Greenwood and A. Earnshaw, *Chemistry of the Elements*, 2nd edn, 1997, pp. 1075–79, Butterworth-Heinemann, ISBN no. 9780750633659.
14 F. Bozso, G. Ertl, M. Grunze and M. Weiss, *J. Catal.*, 1977, **49**, 18.
15 G. Ertl, M. Weiss and S. B. Lee, *Chem. Phys. Lett.*, 1979, **60**, 391.
16 C. Smith, A. K. Hill and L. Torrente-Murciano, *Energy Environ. Sci.*, 2020, **13**, 331.
17 S. D. Minteer, P. Christopher and S. Linic, *ACS Energy Lett.*, 2019, **4**, 163–166.
18 B. D. Matson and J. C. Peters, *ACS Catal.*, 2018, **8**, 1448.
19 N. B. Thompson, M. T. Green and J. C. Peters, *J. Am. Chem. Soc.*, 2017, **139**, 15312.
20 Y. Lee, F. T. Sloane, G. Blondin, K. A. Abboud, R. García-Serres and L. J. Murray, *Angew. Chem., Int. Ed.*, 2015, **54**, 1499.
21 I. Čorić and P. L. Holland, *J. Am. Chem. Soc.*, 2016, **138**, 7200.
22 L. A. Wickramasinghe, T. Ogawa, R. R. Schrock and P. Müller, *J. Am. Chem. Soc.*, 2017, **139**, 9132.
23 J. Fajardo Jr and J. C. Peters, *J. Am. Chem. Soc.*, 2017, **139**, 16105.
24 B. M. Lindley, R. S. van Alten, M. Finger, F. Schendzielorz, C. Würtele, A. J. M. Miller, I. Siewert and S. Schneider, *J. Am. Chem. Soc.*, 2018, **140**, 7922.
25 Y. Sekiguchi, K. Arashiba, H. Tanaka, A. Eizawa, K. Nakajima, K. Yoshizawa and Y. Nishibayashi, *Angew. Chem., Int. Ed.*, 2018, **57**, 9064.
26 Y. Yao, S. Zhu, H. Wang, H. Li and M. Shao, *J. Am. Chem. Soc.*, 2018, **140**, 1496.
27 I. Čorić, B. Q. Mercado, E. Bill, D. J. Vinyard and P. L. Holland, *Nature*, 2015, **526**, 96.
28 J. Rittle and J. C. Peters, *Proc. Natl. Acad. Sci. U. S. A.*, 2013, **110**, 15898.
29 Q. J. Bruch, G. P. Connor, N. D. McMillion, A. S. Goldman, F. Hasanayn, P. L. Holland and A. J. M. Miller, *ACS Catal.*, 2020, **10**, 10826.
30 N. P. Mankad, M. T. Whited and J. C. Peters, *Angew. Chem., Int. Ed.*, 2007, **46**, 5768.
31 Y. Nishibayashi, *Transition Metal-Dinitrogen Complexes: Preparation and Reactivity*, Wiley-VCH Verlag GmbH & Co. KGaA, 2019, DOI: DOI: 10.1002/9783527344260, First published: 25 January 2019, ISBN: 9783527344260.
32 Y. Lee, N. P. Mankad and J. C. Peters, *Proc. Natl. Acad. Sci. U. S. A.*, 2010, **2**, 558.
33 S. E. Creutz and J. C. Peters, *J. Am. Chem. Soc.*, 2014, **136**, 1105.
34 M.-A. Légaré, G. Bélanger-Chabot, R. D. Dewhurst, E. Welz, I. Krummenacher, B. Engels and H. Braunschweig, *Science*, 2018, **359**, 896.
35 M. A. Legare, G. Belanger-Chabot, M. Rang, R. D. Dewhurst, I. Krummenacher, R. Bertermann and H. Braunschweig, *Nat. Chem.*, 2020, **12**, 1076.
36 D. L. J. Broere and P. L. Holland, *Science*, 2018, **359**, 871.
37 T. A. Bazhenova and A. E. Shilov, *Coord. Chem. Rev.*, 1995, **144**, 69.
38 S. Kuriyama, K. Arashiba, K. Nakajima, Y. Matsuo, H. Tanaka, K. Ishii, K. Yoshizawa and Y. Nishibayashi, *Nat. Commun.*, 2016, **7**, 12181.

39 M. Iwamoto, M. Akiyama, K. Aihara and T. Deguchi, *ACS Catal.*, 2017, **7**, 6924.
40 P. J. Hill, L. R. Doyle, A. D. Crawford, W. K. Myers and A. E. Ashley, *J. Am. Chem. Soc.*, 2016, **138**, 13521.
41 G. Ung and J. C. Peters, *Angew. Chem., Int. Ed.*, 2015, **54**, 532.
42 Q. Wang, S. Pan, S. Lei, J. Jin, G. Deng, G. Wang, L. Zhao, M. Zhou and G. Frenking, *Nat. Commun.*, 2019, **10**, 3375.
43 L. Zhao, S. Pan, N. Holzmann, P. Schwerdtfeger and G. Frenking, *Chem. Rev.*, 2019, **119**, 8781.
44 A. Krapp, F. M. Bickelhaupt and G. Frenking, *Chem.–Eur. J.*, 2006, **12**, 9196.
45 G. Ung, J. Rittle, M. Soleilhavoup, G. Bertrand and J. C. Peters, *Angew. Chem., Int. Ed.*, 2014, **53**, 8427.
46 (*a*) V. Lavallo, Y. Canac, C. Präsang, B. Donnadieu and G. Bertrand, *Angew. Chem., Int. Ed.*, 2005, **44**, 5705; (*b*) S. Roy, K. C. Mondal and H. W. Roesky, *Acc. Chem. Res.*, 2016, **49**, 357; (*c*) K. C. Mondal, S. Roy and H. W. Roesky, *Chem. Soc. Rev.*, 2016, **45**, 1080.
47 C. F. Matta and R. J. Boyd, The Quantum Theory of Atoms in Molecules: From Solid State to DNA and Drug Design, *An Introduction to the Quantum Theory of Atoms in Molecules*, Wiley, Hoboken, 2007, ch. 1.
48 (*a*) G. Frenking and F. M. Bickelhaupt, *The Chemical Bond 1. Fundamental Aspects of Chemical Bonding, chap. The EDA Perspective of Chemical Bonding*, Wiley-VCH, Weinheim, 2014, vol. 121; (*b*) L. M. Zhao, M. von Hopffgarten, D. M. Andrada and G. Frenking, *Wiley Interdiscip. Rev.: Comput. Mol. Sci.*, 2018, **8**, 1345; (*c*) L. Zhao, M. Hermann, W. H. E. Schwarz and G. Frenking, *Nat. Rev. Chem.*, 2019, **3**, 48; (*d*) S. Pan and G. Frenking, *Angew. Chem., Int. Ed.*, 2020, **59**, 8756; (*e*) J. Andrés, P. W. Ayers, R. A. Boto, R. Carbó-Dorca, H. Chermette, J. Cioslowski, J. Contreras-García, D. L. Cooper, G. Frenking, C. Gatti, F. Heidar-Zadeh, L. Joubert, Á. M. Pendás, E. Matito, I. Mayer, A. J. Misquitta, Y. Mo, J. Pilmé, P. L. A. Popelier, M. Rahm, E. Ramos-Cordoba, P. Salvador, W. H. E. Schwarz, S. Shahbazian, B. Silvi, M. Solà, K. Szalewicz, V. Tognetti, F. Weinhold and É. L. Zins, *J. Comput. Chem.*, 2019, **40**, 2248; (*f*) W. Yang, K. E. Krantz, L. A. Freeman, D. Dickie, A. Molino, G. Frenking, S. Pan, D. J. D. Wilson and R. J. Gilliard Jr, *Angew. Chem., Int. Ed.*, 2020, **59**, 3850; (*g*) S. M. N. V. T. Gorantla, P. Parameswaran and K. C. Mondal, *J. Comput. Chem.*, 2021, **42**, 1159; (*h*) S. M. N. V. T. Gorantla, S. Pan, K. C. Mondal and G. Frenking, *Chem.–Eur. J.*, 2020, **26**, 14211; (*i*) L. Zhao, S. Pan, M. Zhou and G. Frenking, *Science*, 2019, **365**, eaay5021; (*j*) R. Saha, S. Pan, P. K. Chattaraj and G. Merino, *Dalton Trans.*, 2020, **49**, 1056.
49 (*a*) A. D. Becke, *Phys. Rev. A*, 1988, **38**, 3098; (*b*) J. P. Perdew, *Phys. Rev. B: Condens. Matter Mater. Phys.*, 1986, **33**, 8822; (*c*) S. Grimme, S. Ehrlich and L. Goerigk, *J. Comput. Chem.*, 2011, **32**, 1456; (*d*) S. Grimme, J. Antony, S. Ehrlich and H. Krieg, *J. Chem. Phys.*, 2010, **132**, 154104; (*e*) F. Weigend and R. Ahlrichs, *Phys. Chem. Chem. Phys.*, 2005, **7**, 3297; (*f*) F. Weigend, *Phys. Chem. Chem. Phys.*, 2006, **8**, 1057; (*g*) J. M. Tao, J. P. Perdew, V. N. Staroverov and G. E. Scuseria, *Phys. Rev. Lett.*, 2003, **91**, 146401; (*h*) Y. Zhao and D. G. Truhlar, *J. Chem. Theory Comput.*, 2008, **4**, 1849; (*i*) M. Cossi, N. Rega, G. Scalmani and V. Barone, *J. Comput. Chem.*, 2003, **24**, 669.
50 M. J. Frisch, *et al.*, *Gaussian 16, Revision A.03*, Gaussian, Inc., Wallingford CT, 2016.
51 (*a*) F. Weinhold and C. Landis, *Valency and Bonding, A Natural Bond Orbital Donor – Acceptor Perspective*, Cambridge University Press, Cambridge, 2005; (*b*) C. R. Landis and F. Weinhold, The NBO View of Chemical Bonding, in *The Chemical Bond: Fundamental Aspects of Chemical Bonding*, ed. G. Frenking and S. Shaik, Wiley, 2014, pp. 91–120.
52 K. B. Wiberg, *Tetrahedron*, 1968, **24**, 1083.
53 E. D. Glendening, C. R. Landis and F. Weinhold, *J. Comput. Chem.*, 2013, **34**, 1429.
54 T. Ziegler and A. Rauk, *Theor. Chim. Acta*, 1977, **46**, 1.
55 (*a*) M. Mitoraj and A. Michalak, *Organometallics*, 2007, **26**, 6576; (*b*) M. Mitoraj and A. Michalak, *J. Mol. Model.*, 2008, **14**, 681.
56 (*a*) *ADF2017, SCM, Theoretical Chemistry*, Vrije Universiteit, Amsterdam, The Netherlands, http://www.scm.com; (*b*) G. te Velde, F. M. Bickelhaupt, E. J. Baerends, C. F. Guerra, S. J. A. van Gisbergen, J. G. Snijders and T. Ziegler, *J. Comput. Chem.*, 2001, **22**, 931.
57 (*a*) E. van Lenthe and E. J. Baerends, *J. Comput. Chem.*, 2003, **24**, 1142; (*b*) E. van Lenthe, E. J. Baerends and J. G. Snijders, *J. Chem. Phys.*, 1993, **99**, 4597; (*c*) E. van Lenthe, E. J. Baerends and J. G. Snijders, *J. Chem. Phys.*, 1994, **101**, 9783.